

Rheological behaviour of Carreau liquid past a wedge surface with binary chemical reaction

Kotha Gangadhar¹ , S Venkata Krishna Sarma²
and Ali J Chamkha³

Proc IMechE Part E:

J Process Mechanical Engineering

1–12

© IMechE 2023

Article reuse guidelines:

sagepub.com/journals-permissions

DOI: 10.1177/09544089231207412

journals.sagepub.com/home/pie



Abstract

The time-dependent stream of rheological Carreau nanoliquid carrying microbes through a rotating lodge through porous media in addition to irregular heat source or sink characteristics is the subject of this article. Due to the fact that the Carreau liquid can reveal the rheology of liquids with short-chain suspended particles, liquid crystals, surfactants, and human and animal blood, it is helpful to depict a range of physical problems. The influence of infinite shear rate thickness is combined to provide the mathematical formulation. Both the static and moving physical features are covered in great depth. Prior to using the finite element technique to solve revised equations numerically, pertinent similarity transformations are used to get equations in their dimensionless form. According to the findings of our study, the temperature and the thickness of the thermal boundary layer that corresponds to that temperature both improves the function that the thermal radiation factor plays in shear thickening and thinning liquids. Additionally, a moving wedge has a greater velocity than a static wedge. The thermophoresis factor's rising function is the concentration field. Furthermore, by increasing the Péclet number's magnitudes, the profile of microbes is diminished.

Keywords

Carreau nanoliquid, thermal radiation, motile microorganism, non-uniform heat rise/sink, finite element method

Date received: 6 March 2023; accepted: 13 May 2023

Introduction

Convection indicated particle migration from high to low temperature distributions. When microbes that are denser than water gather at the water surface and a bacterium layer atop lighter liquid was detected as a consequence, the presence of bioconvection was confirmed. But it is commonly acknowledged that when the bacterial density is significantly greater, the bacterial layer collapsed in different convection cells, leading to unstable settings. Nanoparticles bioconvection connects the impulsive structural pattern with buoyant forces, denser self-propelled microorganism characteristics, and nanoparticle density stratification. The microorganism may be classified as gravitaxic, gyrotactic or both types. The growth of microbes significantly improves the suspension of nanoparticles. The microorganism's particles may effectively participate in the creation of chemical and industrial goods like fertiliser, biofuel, ethanol, etc. Kuznetsov hypothesised that the suspension of nanoparticles based on gyrotactic bacteria would include an emotional component.¹ Hussain et al.² conducted research on oxytactic microbes and submicron-phase transition materials for bioconvection in a vertical wavy chamber containing absorbent substances. Waqas et al.³ inspected joule heating and viscous indulgence in magnetised micropolar nanoliquid by means of impermeable stratified surface. Rana et al.⁴ arrived at the

conclusion that a slanting Oldroyd-B liquid by means of mixed convection across a stretchy plane, interaction features and gyrotactic microbes that has the control of suction had neither temperature nor mass. In the stagnation area of a spinning sphere with a magnetic field present, Ali et al.⁵ examined numerically increased heat transfer for bioconvection and mixed convection of tangent hyperbolic nanoliquid stream. Shafiq et al.⁶ conducted research on the bioconvection stream of magnetohydrodynamic (MHD) thixotropic nanoliquid over a perpendicular plane. The bioconvection occurrences are the subject of more research.^{7–15}

Researchers turned attentive in studying liquid stream via wedge-shaped structures because of the many applications that can be found in the fields of engineering and

¹Department of Mathematics, AcharyaNagarjuna University, Guntur, Andhra Pradesh, India

²Department of Mathematics, Dhanekula Institute of Engineering & Technology, Ganguru, Andhra Pradesh, India

³Faculty of Engineering, Kuwait College of Science and Technology, Doha, Kuwait

Corresponding author:

Kotha Gangadhar, Department of Mathematics, AcharyaNagarjuna University Campus, Ongole, Andhra Pradesh, 523001, India.

Email: kgangadharmaths@gmail.com

industrial zones. Wedge stream affects geothermal engineering, heat exchangers, aerodynamics, heat padding, oil recovery, and more. As a result, researchers and writers have concentrated on studying the heat amplification in stream across a wedge. Liquid stream dynamics depend on body shape and form. As a result, heat transmission occurs in liquid passing diverse body types and shapes. Some investigations look into the movement of liquids through wedge-shaped bodies. For instance, Hussain et al.¹⁶ reported a study employing the Eyring-Powell liquid model on chemical reaction stream through a heated permeable wedge. Berrehal et al.¹⁷ explored the stable incompressible laminar hybrid nanoliquid on a radiatively heated moving wedge. Ramesh et al.¹⁸ found the answer for the liquid stream across a moving wedge using an induced magnetic field. Izady et al.¹⁹ examined the analysis for semi-analytical solutions of hybrid nanoliquid stream across a porous stretching or shrinking wedge in two dimensions.

Non-Newtonian liquids violate Newton's thickness rule. The dispensing of antibiotics, food digesting and bio-medical applications like cancer treatment and toxin elimination are all important responsibilities that may be taken into consideration. The thickness of the class-II non-Newtonian liquids is temperature and shear rate dependent. Researchers have demonstrated interest in investigating the thermo-physical characteristics of these liquids during the past 20 years. To compare the non-linearity and complication of the governing equations of non-Newtonian liquids to Newtonian liquids, several fundamental challenges are ignored. Several equations have been proposed for non-Newtonian liquids.

The Carreau non-Newtonian material stream was the subject of the current investigation. The nature of materials whose thickness depends on the rate of shear is elaborated by Carreau's non-Newtonian liquid model. This model can demonstrate thickening and thinning at different shear rates. Khan et al.²⁰ discussion of the Carreau liquid's physical characteristics took non-zero infinite shear rate thickness into account. Maqbool et al. explored ciliated channel mixed convection stream of a Carreau liquid model. Riaz et al.²¹ explored Carreau nanoliquid peristaltic transport in a rectangular channel cross-section.²² Afzal and Akram²³ examined how magnetism and unsteady pounding of Carreau liquid in a narrowed channel affected nanoliquid double-diffusivity confluence.

Heat, mass diffusion and chemical reaction in a permeable medium create gravity-driven transport phenomena. Due to its uses in the chemical industry, solar water collection systems and food processing, investigations on these phenomena are very important. Additionally, chemical reactions that occur on moving surfaces between an external mass and a liquid are very important to the chemical engineering sector. There are two further classifications for chemical reactions: homogeneous and heterogeneous. A reaction is considered homogeneous if it occurs consistently across the course of a certain phase; otherwise, it is considered heterogeneous. Given that it

is essential to both mechanical and chemical engineering, several scholars examined how homogenous chemical reaction rates of order one affect vertical surfaces like plates and cylinders. Azam²⁴ numerically investigated the axisymmetric stream of a chemically reactive Sutterby nanoliquid. Sithole et al.²⁵ performed an analysis of heat and mass transport of pair stress nanoliquid streams in a magneto-porous media while taking into account radiant heat and heat production. The effects of Marangoni convection Casson nanoliquid stream in gyrotactic bacteria were investigated by Madhukesh et al.²⁶ on the porous sheet. Sivasankaran et al. studied MHD nanoliquid squeezed stream across two surfaces theoretically.²⁷ In the investigations,²⁸⁻³⁶ further recent developments pertinent to the intended topic may be discovered.

The previous studies served as the impetus for the ongoing project, which aims to provide analytical results on the properties of bioconvection in the precarious 2-D Falkner-Skan stream of Carreau nanoliquid through a stationary or shifting wedge. These solutions will be based on the inspiration provided by the previous studies. The energy equation also takes into account thermal radiation and non-uniform heat sources and sinks. Additionally, a chemical reaction results in a further intricate substantial issue. The Carreau thickness model is a key generalised Newtonian liquid that explains shear depletion and thickness. As the power law index n is one and We is null, the concept is simplified down to a liquid with viscosity. By applying the relevant conversions, the controlling non-linear boundary-layer equations are changed into non-linear ordinary differential equations. The resulting equations are resolved by employing the effective numerical approach known as the finite element technique. With extremely excellent agreement, the new findings are compared to previous research in a limited example.

Mathematical formulation

Two-dimensional inviscid Carreau nanoliquid stream through a wedge geometry by gyrostatically motile microbes. Radiation and heat distribution are addressed. We considered stream over the wedge with $U_w(x_0, t_0) = b_0 x_0^m / (1 - c_0 t_0)$, where $U_w(x_0, t_0) > 0$ is for stretching velocity and contracting wedge is as $U_w(x_0, t_0) < 0$. $U_b(x_0, t_0) = a_0 x_0^m / (1 - c_0 t_0)$, is the free stream, and a_0, b_0, c_0 . The m is the positive constant. Wedge angle is $\Omega = \beta\pi$ in which $\beta = 2m / (1 + m)$ is the wedge angle stricture (check the Figure 1 below).

Cauchy stress tensor $\tilde{\tau}$ for Carreau liquid method is designed by Carreau²⁸:

$$\tilde{\tau} = -pI_0 + \mu B_0, \quad \mu = \mu_0 (1 + (\Gamma_0 \tilde{\gamma})^2)^{0.5(n-1)}. \quad (1)$$

Power law index range $0 < n < 1$ presents the dilatant or shear thickening liquids and $n > 1$ display the dilatant or shear thickness liquids. Therefore

$$\tilde{\gamma} = \sqrt{0.5(\Omega_i \Omega_j \tilde{\gamma}_{ij} \tilde{\gamma}_{ji})} = \sqrt{0.5(tr(B_0^2))}, \quad (2)$$

where p is the pressure, I_0 the identity tensor, n the power law index, B_0 the first Rivlin-Ericksen constant, Ω the time material constant, $\tilde{\gamma}$ the share rate and μ_0 the zero share rate. There is no correlation between the way in which the volume percentage of nanoparticles moves and the swimming direction of the microbe.

Heat and the thickness of gyrotactic microbes are T_w and N_w ; the adjacent temperature distribution is T_∞ and volumetric nanoparticles concentration and motile microbes are C_∞ and N_∞ , respectively. The final terms are [Khan et al.²⁹]:

$$\frac{\partial u_0}{\partial x_0} + \frac{\partial v_0}{\partial y_0} = 0, \quad (3)$$

$$\begin{aligned} \frac{\partial u_0}{\partial t_0} + u_0 \frac{\partial u_0}{\partial x_0} + v_0 \frac{\partial u_0}{\partial y_0} &= \frac{\partial U_b}{\partial t_0} + U_b \frac{\partial U_b}{\partial x_0} \\ &+ v \frac{\partial^2 u_0}{\partial y_0^2} \left(1 + \Omega^2 \left(\frac{\partial u_0}{\partial y_0} \right)^2 \right)^{0.5(n-1)} - \frac{v\varphi}{K^*} u_0 + \\ &\frac{1}{\rho_f} \left[(1 - C_\infty) \rho_f \beta_0 g_0 (T - T_\infty) - (\rho_p - \rho_f) g_0 (C - C_\infty) \right], \end{aligned} \quad (4)$$

$$\begin{aligned} \frac{\partial T}{\partial t_0} + u_0 \frac{\partial T}{\partial x_0} + v_0 \frac{\partial T}{\partial y_0} &= \alpha_m \frac{\partial^2 T}{\partial y_0^2} \\ &+ \frac{(\rho c)_f}{(\rho c)_p} \left(D_B \frac{\partial C}{\partial y_0} \frac{\partial T}{\partial y_0} + \frac{D_T}{T_\infty} \left(\frac{\partial T}{\partial y_0} \right)^2 \right) \\ &- \frac{1}{\rho c_p} \frac{\partial q_r}{\partial y_0} + q''', \end{aligned} \quad (5)$$

$$\begin{aligned} \frac{\partial C}{\partial t_0} + u_0 \frac{\partial C}{\partial x_0} + v_0 \frac{\partial C}{\partial y_0} &= D_B \frac{\partial^2 C}{\partial y_0^2} + \frac{D_T}{T_\infty} \frac{\partial^2 T}{\partial y_0^2} \\ &- k_0 (C - C_\infty)^2, \end{aligned} \quad (6)$$

$$\begin{aligned} \frac{\partial N}{\partial t_0} + u_0 \frac{\partial N}{\partial x_0} + v_0 \frac{\partial N}{\partial y_0} &= D_m \frac{\partial^2 N}{\partial y_0^2} \\ &- \frac{\tilde{b} W_c}{(C_w - C_\infty)} \left[\frac{\partial}{\partial y_0} \left(N \frac{\partial C}{\partial y_0} \right) \right], \end{aligned} \quad (7)$$

where u_0 and v_0 are in x_0 and y_0 directions, correspondingly; volumetric absorption of nanoparticle is C ; thermal diffusivity is α_m ; and $(\rho c)_f$, $(\rho c)_p$ are base liquid heat capability and nanoparticle effective heat capability.

Subjected boundary settings are

$$\begin{aligned} u_0 &= U_w, v_0 = 0, T = T_w, C = C_w, \\ N &= N_w, \text{ as } y_0 = 0, \end{aligned} \quad (8)$$

$$\begin{aligned} u_0 &\rightarrow U_b, T \rightarrow T_\infty, C \rightarrow C_\infty, N \rightarrow N_\infty \text{ as } \\ y_0 &\rightarrow \infty. \end{aligned} \quad (9)$$

Rosseland approximation, $q_r = -\frac{4\sigma_0}{3\kappa^*} \frac{\partial T^4}{\partial y_0}$ (σ_0 is Stefan-Boltzman constant and κ^* the absorption coefficient). T^4 may be expressed by Taylor's series. Rising T^4 about T_∞ and neglecting relatively high elements takes $T^4 = 4T_\infty^3 T - 3T_\infty^4$. Under such supposition we obtain $q_r = -\frac{16T_\infty^3 \sigma_0}{3\kappa^*} \frac{\partial T}{\partial y_0}$.

From equation (4), q''' is the variable heat generation as told by Mumraiz et al.³⁰

$$q''' = \frac{kU_w(x_0, t_0)}{x_0 v} [B_1(T_w - T_\infty)\omega' + (T - T_\infty)B_2]. \quad (10)$$

Heat production is $(B_1, B_2) > 0$ and heat absorption is $(B_1, B_2) < 0$.

Suitable transformations are

$$\begin{aligned} \xi &= y_0 \sqrt{\frac{(m+1)U_b}{2vx_0}}, \Psi = \sqrt{\frac{2vx_0 U_b}{m+1}} \omega(\xi), \theta(\xi) = \frac{T - T_\infty}{T_w - T_\infty}, \\ \phi(\xi) &= \frac{C - C_\infty}{C_w - C_\infty}, \Upsilon(\xi) = \frac{N - N_\infty}{N_w - N_\infty}. \end{aligned} \quad (11)$$

Equation (3) has been proven correct, and results from equations (4) to (9) are as follows [Khan et al.²⁹]:

$$\begin{aligned} (1 + nWe^2(\omega'')^2)(1 + nWe^2(\omega'')^2)^{0.5(n-3)} \omega''' &- \beta(\omega'^2 - 1) \\ &+ \omega\omega'' - k_p\omega' - A(\omega' + 0.5\xi\omega'' - 1) \\ &+ \Lambda_1(\theta - Nr\phi - Rb\Upsilon) = 0, \end{aligned} \quad (12)$$

$$\begin{aligned} \left(1 + \frac{4Rd}{3} \right) \theta'' + Pr \left(\omega\theta' - \frac{A}{2} \xi \theta' \right) &+ Nb\theta'\phi' + Nt\theta^2 \\ &+ B_1\omega' + B_2\theta = 0, \end{aligned} \quad (13)$$

$$\phi'' + PrLe \left(\omega\phi' - \frac{A}{2} \xi \phi' \right) + \frac{Nt}{Nb} \theta'' - KrLePr\phi^2 = 0, \quad (14)$$

$$\Upsilon'' + Lb \left(\omega\Upsilon' - \frac{A}{2} \xi \Upsilon' \right) - Pe(\phi''(\Upsilon + \delta_1) + \Upsilon'\phi') = 0. \quad (15)$$

The boundary restrictions are

$$\begin{aligned} \omega(0) &= 0, \omega'(0) = \lambda, \theta(0) = 1, \phi(0) = 1, \\ \Upsilon(0) &= 1, \end{aligned} \quad (16)$$

$$\omega'(\infty) \rightarrow 1, \theta(\infty) \rightarrow 0, \phi(\infty) \rightarrow 0, \Upsilon(\infty) \rightarrow 0. \quad (17)$$

The dimensionless variables are $k_p = \frac{v\varphi}{K^*a}$ is the porosity factor, $We = \sqrt{\frac{\Omega^2(m+1)U_b^3}{2v}}$ Weissenberg number, $\Lambda_1 = \frac{\beta_0(1-C_\infty)(T_w-T_\infty)}{(m+1)U_b^2}$ - mixed convection number,

$Nr = \frac{(\rho_p - \rho_f)(C_w - C_\infty)}{(1 - C_\infty)(T_w - T_\infty)\beta_0}$ – the buoyancy ratio number,
 $Rb = \frac{\gamma^*(\rho_m - \rho_f)(N_w - N_\infty)}{(1 - C_\infty)(T_w - T_\infty)\beta_0}$ – the bioconvection Rayleigh number, $Nb = \frac{\tau D_B(C_w - C_\infty)}{v}$ – the Brownian motion factor,
 $Nt = \frac{\tau D_T(T_w - T_\infty)}{v T_\infty}$ – the thermophoresis factor, $Pr = \frac{v}{\alpha_m}$ – the Prandtl number, $Le = \frac{\alpha}{D_B}$ – the Lewis number, $Rd = \frac{4\sigma_0 T_\infty^3}{k k^*}$ – the radiation factor, $Pe = \frac{\dot{h} W_c}{D_m}$ – the Peclet number, $Lb = \frac{v}{D_m}$ – the bioconvection Lewis number, $\delta_1 = \frac{N_\infty}{N_w - N_\infty}$ – the motile microorganism difference factor, $Re_x = \frac{x_0 U_b}{v}$ – the Reynolds number and $Kr = \frac{k_0}{a}$ – the chemical reaction factor.

Skin friction, local Nusselt number, local Sherwood number and thickness of local motile number are the physical elements of momentum, thermal allocation, volume fraction of absorption and motile microbe swimming (C_f , Nu , Sh and Nh) that are of primary importance in the article.

$$C_f = \frac{\tau_w}{\rho_f U_b^2} \Big|_{y_0=0}, \quad Nu = \frac{x_0 q_j}{k(T_w - T_\infty)}, \quad (18)$$

$$Sh = \frac{x_0 q_w}{D_B(C_w - C_\infty)}, \quad Nh = \frac{x_0 q_m}{D_m(N_w - N_\infty)},$$

The surface shear stress, denoted by τ_w , the surface heat and mass fluxes, denoted by q_j , and q_w , respectively, and the motile thickness, denoted by q_m , are defined:

$$\tau_w = \mu \frac{\partial u_0}{\partial y_0} \left(1 + \frac{n \Gamma_0^2}{\sqrt{2}} \left(\frac{\partial u_0}{\partial y_0} \right)^2 \right)^{0.5(n-1)} \Big|_{y_0=0},$$

$$q_j = \left(-k \left(\frac{\partial T}{\partial y_0} \right) + q_r \right) \Big|_{y_0=0}, \quad (19)$$

$$q_w = -D_B \left(\frac{\partial C}{\partial y_0} \right) \Big|_{y_0=0}, \quad q_m = -D_m \left(\frac{\partial N}{\partial y_0} \right) \Big|_{y_0=0}. \quad (20)$$

In dimensionless outline, equation (18) gives

$$C_f Re^{1/2} (2 - \beta)^{0.5} = \omega''(0) \left(1 + We^2 (\omega''(0))^2 \right)^{0.5(n-1)},$$

$$Nu Re^{1/2} (2 - \beta)^{0.5} = - \left(1 + \frac{4Rd}{3} \right) \theta'(0),$$

$$Sh Re^{1/2} (2 - \beta)^{0.5} = - \phi'(0),$$

$$Nh Re^{1/2} (2 - \beta)^{0.5} = - Y'(0). \quad (21)$$

Numerical solution

The finite element method

Implementation of the variational finite element means for numerical evaluation of equations (12) to (15) with boundary settings (equations (16)–(17)). Finite element techniques are better at numerically solving ordinary and partial differential equations. The finite element method has these steps.

1. Finite element discretisation
 Discretisation is the separation of the domain into finite subdomains. Subdomains are elements. Components are mentioned.
2. Element equation production
 (a) Following the removal of a scale area from the grid, the finite difference solution to the task at hand is then constructed on top of the scale area.
 (b) Replacing an estimate of the variational issue solution into the system yields the element equations.
 (c) Using the element interpolation functions, the stiffness matrix, also known as the Assembly of element equations
 With the implementation of permanence criteria between components, the resultant mathematical formulae are generated. The global finite element model has several algebraic equations that govern the domain.
3. Implementation of boundary settings
 When the combined results are obtained, the required and natural boundary settings are applied to them.
4. Elucidation of assembled equations
 Any numerical methodology, such as the Gauss elimination method, LU decomposition method, etc., may be used to solve the collected equations that have been produced in this manner. The form functions used to approximate real functions are a crucial factor to take into account.

In order to decipher the set of non-linear ordinary differential equations (12) to (15) in conjunction with the boundary settings (equations (16)–(17)), we will begin by making the assumption that

$$\frac{d\omega}{d\xi} = h, \quad (22)$$

The equations (12) to (15) are reduced to

$$\left(1 + nWe^2 (h')^2 \right) \left(1 + nWe^2 (h')^2 \right)^{0.5(n-3)} h'' - \beta (h^2 - 1) + \omega h' - k_p h - A(h + 0.5\xi h' - 1) + \Lambda_1 (\theta - Nr\phi - RbY) = 0, \quad (23)$$

$$\left(1 + \frac{4Rd}{3} \right) \theta'' + Pr \left(\omega \theta' - \frac{A}{2} \xi \theta' \right) + Nb \theta' \phi' + Nt \theta^2 + B_1 h + B_2 \theta = 0, \quad (24)$$

$$\phi'' + Pr Le \left(\omega \phi' - \frac{A}{2} \xi \phi' \right) + \frac{Nt}{Nb} \theta'' - Kr Pr Le \phi^2 = 0, \quad (25)$$

$$Y'' + Lb \left(\omega Y' - \frac{A}{2} \xi Y' \right) - Pe (\phi'' (Y + \delta_1) + Y' \phi') = 0. \quad (26)$$

The boundary settings forms

$$\omega(0) = 0, h(0) = \lambda, \theta(0) = 1, \phi(0) = 1, \Upsilon(0) = 1, \quad (27)$$

$$h(\infty) \rightarrow 1, \theta(\infty) \rightarrow 0, \phi(\infty) \rightarrow 0, \Upsilon(\infty) \rightarrow 0. \quad (28)$$

Variational formulation

The discretisation pattern over a typical linear element ($d, d+1$) that is related with equations (16) to (20) is determined by:

$$\int_{\xi_d}^{\xi_{d+1}} w_1 \left(\frac{d\omega}{d\xi} - h \right) d\xi = 0, \quad (29)$$

$$\int_{\xi_d}^{\xi_{d+1}} w_2 \left(\left(1 + nWe^2(h')^2 \right) \left(1 + nWe^2(h'')^2 \right)^{0.5(n-3)} h'' - \beta(h^2 - 1) \right) d\xi = 0, \quad (30)$$

$$\int_{\xi_d}^{\xi_{d+1}} w_3 \left(\left(1 + \frac{4Rd}{3} \right) \theta'' + Pr \left(\omega \theta' - \frac{A}{2} \xi \theta' \right) + Nb \theta' \phi' + Nt \theta'^2 + B_1 h + B_2 \theta \right) d\xi = 0, \quad (31)$$

$$\int_{\xi_d}^{\xi_{d+1}} w_4 \left(\phi'' + PrLe \left(\omega \phi' - \frac{A}{2} \xi \phi' \right) + \frac{Nt}{Nb} \theta'' - KrPrLe \phi^2 \right) d\xi = 0, \quad (32)$$

$$\int_{\xi_d}^{\xi_{d+1}} w_5 \left(\Upsilon'' + Lb \left(\omega \Upsilon' - \frac{A}{2} \xi \Upsilon' \right) - Pe(\phi''(\Upsilon + \delta_1) + \Upsilon' \phi') \right) d\xi = 0, \quad (33)$$

where $\omega_1, \omega_2, \omega_3, \omega_4$ and ω_5 are arbitrary test functions and are also the types in ω, h, θ, ϕ and Υ , accordingly.

Finite element formulation

By introducing finite-element approximations of the type into the aforementioned equations, the finite element

model is produced.

$$\omega = \sum_{j=1}^2 \omega_j \Delta_j, h = \sum_{j=1}^2 h_j \Delta_j, \theta = \sum_{j=1}^2 \theta_j \Delta_j, \quad (34)$$

$$\phi = \sum_{j=1}^2 \phi_j \Delta_j, \Upsilon = \sum_{j=1}^2 \Upsilon_j \Delta_j,$$

with $\omega_1 = \omega_2 = \omega_3 = \omega_4 = \omega_5 = \Delta_i (i = 1, 2, 3)$.

In which Δ_i are the shape functions for a typical element (ξ_d, ξ_{d+1}) and are termed:

$$\Delta_1^e = \frac{(\xi_{d+1} + \xi_d - 2\xi)(\xi_{d+1} - \xi)}{(\xi_{d+1} - \xi_d)^2}, \Delta_2^e = \frac{4(\xi - \xi_d)(\xi_{d+1} - \xi)}{(\xi_{d+1} - \xi_d)^2},$$

$$\Delta_3^e = \frac{(\xi_{d+1} + \xi_d - 2\xi)(\xi - \xi_d)}{(\xi_{d+1} - \xi_d)^2}, \xi_d \leq \xi \leq \xi_{d+1}. \quad (35)$$

Thus, the equations' finite element model is

$$\begin{bmatrix} [H^{11}] & [H^{12}] & [H^{13}] & [H^{14}] & [H^{15}] \\ [H^{21}] & [H^{22}] & [H^{23}] & [H^{24}] & [H^{25}] \\ [H^{31}] & [H^{32}] & [H^{33}] & [H^{34}] & [H^{35}] \\ [H^{41}] & [H^{42}] & [H^{43}] & [H^{44}] & [H^{45}] \\ [H^{51}] & [H^{52}] & [H^{53}] & [H^{54}] & [H^{55}] \end{bmatrix} \begin{bmatrix} \omega \\ h \\ \theta \\ \phi \\ \Upsilon \end{bmatrix} = \begin{bmatrix} \{r^1\} \\ \{r^2\} \\ \{r^3\} \\ \{r^4\} \\ \{r^5\} \end{bmatrix}, \quad (36)$$

where $[H^{mn}]$ and $[r^m] (m, n = 1, 2, 3, 4, 5)$ are termed as

$$H_{ij}^{11} = \int_{\xi_d}^{\xi_{d+1}} \Delta_i \frac{d\Delta_j}{d\xi} d\xi, H_{ij}^{12} = - \int_{\xi_d}^{\xi_{d+1}} \Delta_i \Delta_j d\xi, H_{ij}^{13} = H_{ij}^{14} = H_{ij}^{15} = 0,$$

$$H^{22} = -(1 + nWe^2 \bar{h}^{-2})(1 + nWe^2 \bar{h}^{-2})^{0.5(n-3)} \int_{\xi_d}^{\xi_{d+1}} \frac{d\Delta_i}{d\xi} \frac{d\Delta_j}{d\xi} d\xi$$

$$+ (\bar{\omega} - 0.5A\xi) \int_{\xi_d}^{\xi_{d+1}} \Delta_i \frac{d\Delta_j}{d\xi} d\xi - (\beta \bar{h} + k_p + A) \int_{\xi_d}^{\xi_{d+1}} \Delta_i \Delta_j d\xi, H^{21} = 0,$$

$$H^{23} = \Lambda_1 \int_{\xi_d}^{\xi_{d+1}} \Delta_i \Delta_j d\xi, H^{24} = -\Lambda_1 Nr \int_{\xi_d}^{\xi_{d+1}} \Delta_i \Delta_j d\xi, H^{25} = -Rb\Lambda_1 \int_{\xi_d}^{\xi_{d+1}} \Delta_i \Delta_j d\xi,$$

$$H^{33} = -\left(1 + \frac{4Rd}{3}\right) \int_{\xi_d}^{\xi_{d+1}} \frac{d\Delta_i}{d\xi} \frac{d\Delta_j}{d\xi} d\xi + \left(Pr\bar{\omega} - \frac{PrA}{2}\xi + Nb\bar{\phi}' + Nt\bar{\theta}'\right) \int_{\xi_d}^{\xi_{d+1}} \Delta_i \frac{d\Delta_j}{d\xi} d\xi + B_2 \int_{\xi_d}^{\xi_{d+1}} \Delta_i \Delta_j d\xi,$$

$$H^{32} = B_1 \int_{\xi_d}^{\xi_{d+1}} \Delta_i \Delta_j d\xi, H^{31} = H^{34} = H^{35} = 0,$$

$$H^{44} = - \int_{\xi_d}^{\xi_{d+1}} \frac{d\Delta_i}{d\xi} \frac{d\Delta_j}{d\xi} d\xi + LePr \left(\bar{\omega} - \frac{A}{2}\xi\right) \int_{\xi_d}^{\xi_{d+1}} \Delta_i \frac{d\Delta_j}{d\xi} d\xi - LePrKr\bar{\phi}' \int_{\xi_d}^{\xi_{d+1}} \Delta_i \Delta_j d\xi, H^{43} = -\frac{Nt}{Nb} \int_{\xi_d}^{\xi_{d+1}} \frac{d\Delta_i}{d\xi} \frac{d\Delta_j}{d\xi} d\xi,$$

$$H^{41} = H^{42} = H^{45} = 0,$$

$$H^{55} = - \int_{\xi_d}^{\xi_{d+1}} \frac{d\Delta_i}{d\xi} \frac{d\Delta_j}{d\xi} d\xi + Lb \left(\bar{\omega} - \frac{A}{2}\xi + Le\bar{\phi}'\right) \times \int_{\xi_d}^{\xi_{d+1}} \Delta_i \frac{d\Delta_j}{d\xi} d\xi,$$

$$H^{54} = -Pe(\bar{Y} + \delta_1) \int_{\xi_d}^{\xi_{d+1}} \Delta_i \Delta_j d\xi, H^{51} = H^{52} = H^{53} = 0,$$

and

$$r^1 = 0,$$

$$r^2 = -\left(1 + nWe^2 \bar{h}^{-2}\right) \left(1 + nWe^2 \bar{h}^{-2}\right)^{0.5(n-3)} \left[\Delta_i \frac{dh}{d\xi}\right]_{\xi_d}^{\xi_{d+1}} - (1 + A) \int_{\xi_d}^{\xi_{d+1}} \Delta_i d\xi,$$

$$r^3 = -\left(1 + \frac{4Rd}{3}\right) \left[\Delta_i \frac{d\theta}{d\xi}\right]_{\xi_d}^{\xi_{d+1}},$$

$$r^4 = -\frac{Nt}{Nb} \left[\Delta_i \frac{d\theta}{d\xi}\right]_{\xi_d}^{\xi_{d+1}} - \left[\Delta_i \frac{d\phi}{d\xi}\right]_{\xi_d}^{\xi_{d+1}},$$

$$r^5 = -\left[\Delta_i \frac{dY}{d\xi}\right]_{\xi_d}^{\xi_{d+1}} - Pe(\bar{Y} + \delta_1) \left[\Delta_i \frac{d\phi}{d\xi}\right]_{\xi_d}^{\xi_{d+1}}.$$

Validation of results

Comparing results to prior research to gauge the correctness of the current finite element method (FEM) code, the findings are shown in Table 1. The tables suggest that there is a great agreement between the current findings and the data that has already been published, demonstrating the reliability of the FEM code.

Results and discussion

The acquired numerical and graphical findings for the shear thickening ($n > 1$) and shear thinning ($0 < n < 1$) scenarios are reported here. The outcomes are produced using the finite element approach. Impacts of new physical factors like porosity factor k_p , buoyancy ratio factor Nr , mixed convection factor Λ_1 , bioconvection Rayleigh number Rb , Weissenberg number We , thermophoresis factor Nt , Brownian motion factor Nb , radiation factor Rd , heat generation or absorption factors B_1, B_2 , Peclet factor Pe and bioconvection Lewis factor Lb are all well investigated. The parametric values other than varied one are taken as $Pr = 6.2, \sigma = 2.0, Nt = 0.1, Rd = 0.2, Nb = 0.1, Le = 10.0, Lb = 1.0, Pe = 0.2, Kr = 0.2, We = 5.0, \beta = 0.2, A = 0.1, \Lambda_1 = 0.2, Nr = 0.2, B_1 = 0.1, Rb = 0.1$ and $B_2 = 0.1$. The outcomes are discussed below.

Figure 2 depicts the wedge angle factor's β role in the velocity profile ω' for shear thickening and thinning liquids in a rotating blade, with variations in the parameter of 0.0, 0.4, 0.8 and 1.2. These graphs show how the wedge angle factor increases liquid velocity. Keep in mind that the Hartree pressure gradient factor $\beta = \frac{\Omega}{\pi}$

Table 1. Comparison of $(2 - \beta)^{1/2} Re^{-1/2} Nu$ for variation of Pr and β when $n = 1$ and $Nt = Rd = Nb = B_1 = B_2 = Nr = Rb = \lambda = 0$.

Pr	$\beta = 0.0$			$\beta = 0.3$		
	Khan et al. ²⁹	Muhammad et al. ³⁰	Present outcomes	Khan et al. ²⁹	Muhammad et al. ³⁰	Present outcomes
0.1	0.198129	0.198127	0.1980314	0.209152	0.209152	0.2090754
0.3	0.303718	0.303710	0.3037174	0.327829	0.327829	0.3278290
0.6	0.391675	0.391674	0.3916751	0.428924	0.428924	0.4289244
0.72	0.418091	0.418092	0.4180913	0.459551	0.459551	0.4595511
1.0	0.469600	0.469601	0.4696000	0.519519	0.519519	0.5195184
2.0	0.597234	0.597239	0.5972339	0.669045	0.669045	0.6690446
6.0	0.867278	0.867279	0.8672775	0.987268	0.987268	0.9872675
10.0	1.029747	1.029749	1.0297472	1.179130	1.179130	1.1791300

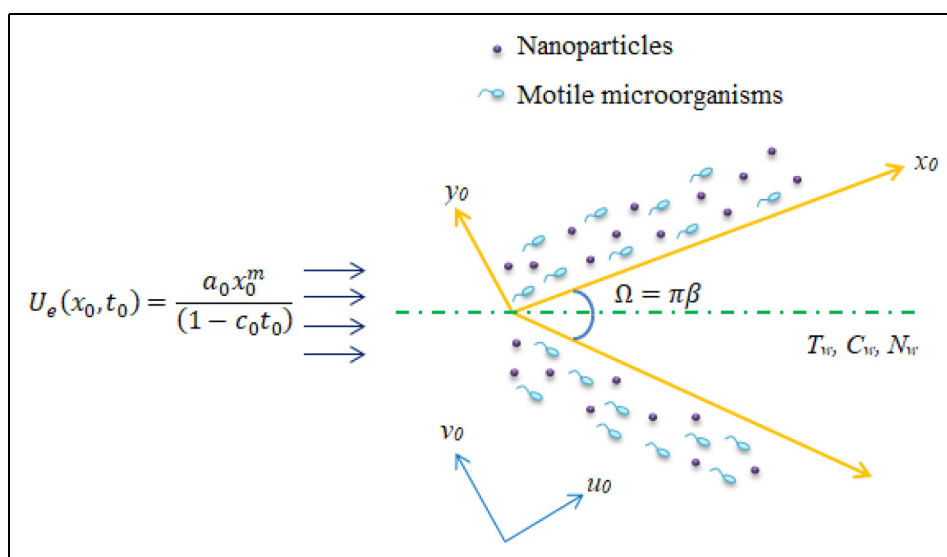


Figure 1. Schematic view of the problem.

corresponds to the wedge angle factor. If the pressure gradient β is positive or negative from the viewpoint of White,³⁷ this indicates that the stream will gain speed as it moves down the surface. When the pressure gradient is unfavourable, as seen by negative values, the stream will be decelerating. Additionally, $\beta = 1$ ($m = 1$) corresponds to boundary layer stream at the stagnation position of a perpendicular even plate, whereas $\beta = 0$ ($m = 0$) corresponds to boundary sheet stream across a flat plate. Additionally, it is shown that the shear-thinning case results in a higher velocity than the shear-thickening case.

Figure 3 illustrates the Weissenberg number (We) effect on the velocity profile in support of shear thickening and thinning. The velocity profile is shown to be shrinking the whole domain throughout a range of We values. Physically, We employs the viscoelastic streams to explore the interaction between elastic and viscous forces. For larger We , velocity drops due to increased liquid relaxation time because this resistance causes the liquid's particles to stream, hence, the velocity diminishes. For all Weissenberg numbers, shear thickening has a lower velocity than shear thinning. Figure 4 shows how the permeability factor kp affects velocity profiles of shear thinning and thickening. Because the surface porosity increases with increasing porosity, there is

a decreasing trend in the velocity curves for $kp = 0.0, 0.2, 0.4$ and 0.6 . Additionally, it should be noted that the findings are more significant for lower porosity factor values than for higher kp values.

Figure 5 shows the shear-thickening and shear-thinning effects of the mixed convection factor Λ_1 on the velocity profile of a moving wedge. The force convection stream location ($\Lambda_1 = 0$) beneath the permeable moving wedge has the least amount of nanoliquid stream along the stretched sheet. The convection current significantly increases the stream of nanoliquid at the heated stretching surface location ($\Lambda_1 > 0$). Along the moving wedge stream direction, the natural convection current predominated over the forced convection of the liquid molecules and nanoparticles. The increased mixed convection factor results in the shear thickening decreases from the shear thinning.

According to the effect of the wedge moving factor, Figure 6 illustrates the temperature for dilatant ($n = 1.5$) and pseudo-plastic ($n = 0.5$) materials. A moving wedge results in a higher liquid velocity (i.e. positive values of λ) than a static wedge ($\lambda = 0$). It is crucial to note that λ is the constant moving wedge factor and that values of $\lambda > 0$ and $\lambda < 0$ correspond to moving wedges that move in

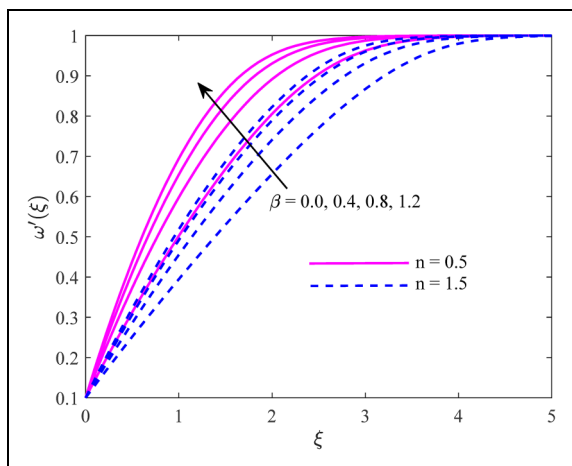


Figure 2. Velocity $\omega'(\xi)$ with various values of β .

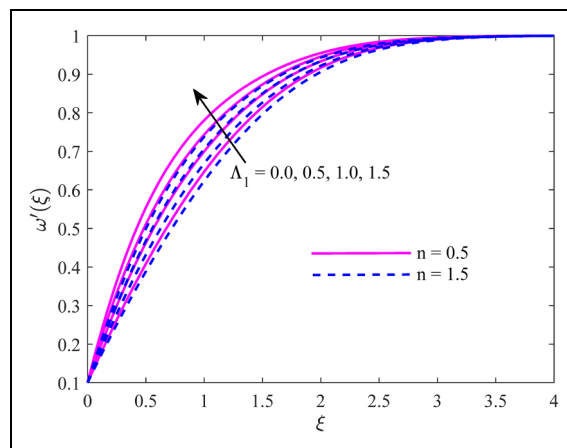


Figure 5. Velocity $\omega'(\xi)$ with various values of Λ_1 .

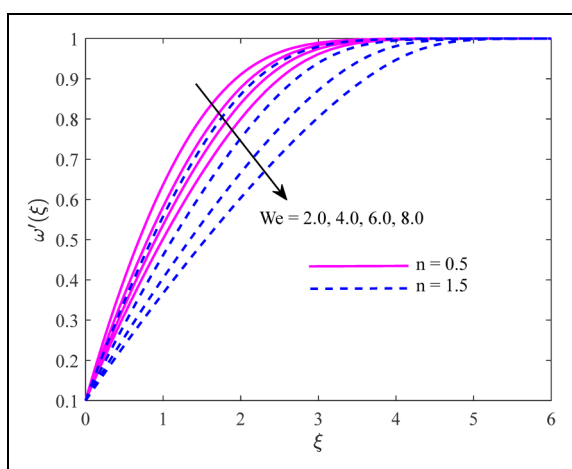


Figure 3. Velocity $\omega'(\xi)$ with various values of We .

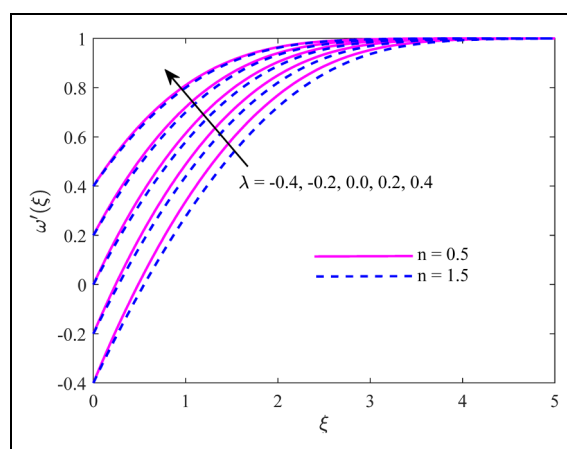


Figure 6. Velocity $\omega'(\xi)$ with various values of λ .

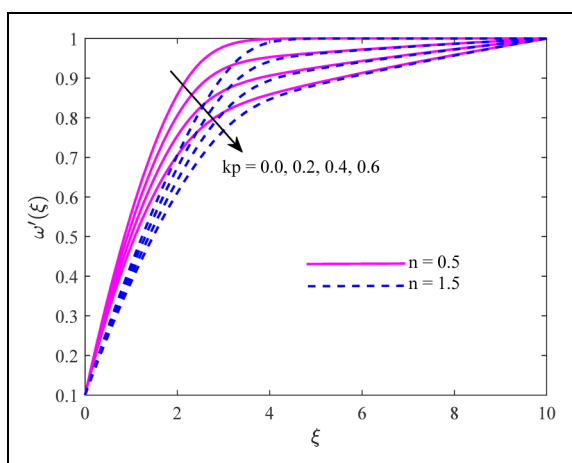


Figure 4. Velocity $\omega'(\xi)$ with various values of k_p .

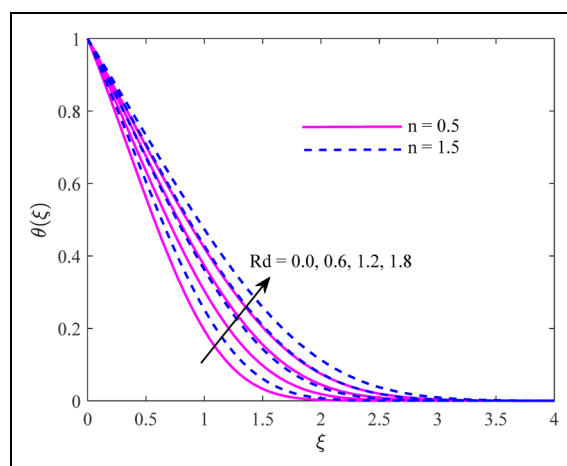


Figure 7. Velocity $\theta(\xi)$ with various values of Rd .

directions that are similar to and different from the free stream velocity, respectively.

Figure 7 shows how Rd affects the temperature profile of dilatant ($n = 1.5$) and pseudo-plastic ($n = 0.5$) nanofluids. An increase in heat radiation increases the conduction impact and increases the thickness of the thermal

layer. Every location distant from the peak permeable surface is now seeing an increase in temperature. Heating liquid molecules and nanoparticles increases the dispersal. The effects of shear-thickening liquid are more obvious than shear-thinning liquid. A non-zero value of Rd shows that thermal radiation has an influence

Table 2. Tabular results for skin-friction coefficient.

We	kp	λ	Nr	Rb	β	A	Λ_1	$C_f Re^{1/2} (2 - \beta)^{0.5}$	
								n = 0.5	n = 1.5
0.2	0.1	0.1	0.2	0.1	0.2	0.1	0.2	0.673589	0.675125
0.4								0.661566	0.667680
0.6								0.643449	0.656938
0.8								0.621341	0.644387
0.5	0.0							0.744986	0.759553
	0.2							0.573682	0.579892
	0.4							0.451291	0.454139
	0.6							0.368763	0.370257
	0.1	0.0						0.702762	0.714672
		0.1						0.653140	0.662622
		0.2						0.596684	0.603833
		0.3						0.533389	0.538419
		0.1	0.0					0.659919	0.669557
			0.4					0.646331	0.655661
			0.8					0.632629	0.641666
			1.2					0.618811	0.627570
			0.2	0.0				0.660610	0.670350
				0.2				0.645627	0.654856
				0.4				0.630474	0.639213
				0.6				0.615149	0.623417
				0.1	0.1			0.565899	0.571934
					0.3			0.727423	0.740805
					0.5			0.850124	0.872302
					0.7			0.949966	0.981897
					0.2	0.0		0.604979	0.612535
						0.2		0.697914	0.709533
						0.4		0.779097	0.795565
						0.6		0.851422	0.873442
						0.1	0.0	0.569434	0.576325
							0.4	0.730975	0.743664
							0.8	0.872095	0.893048
							1.2	0.997318	1.028915

on the stream, while $Rd = 0$ implies that there is no radiation in the stream scenario.

In Supplemental Figure 8 we can see the thermophoresis factor's Nt reaction on the temperature distributions for liquids that are thickening and thinning under shear. This graph shows how increasing the thermophoresis factor results in improved temperature profiles. Physically, when Nt increases, the thermophoresis energy increases, tending to transfer nanoparticles from hot to cold regions and so increasing the amplitude of the concentration profile. In contrast to shear-thinning liquids, the consequences for shear-thickening liquids are more obvious.

Shear-thickening and shear-thinning liquids each have their own unique set of temperature profile variations that may be plotted against the Brownian motion factor Nb and are seen in Supplemental Figure 9. Because Brownian motion has the effect of speeding up the random motion of nanoparticles, these nanoparticles experience rapid striking as a result of their erratic movement; hence their kinetic energy is transformed into heat energy resulting in temperature rise across the entire thermal boundary system. Nb values ranged from 0.1 to

1.3. The effects for shear-thinning liquids are lowered in comparison with that of shear thickening.

Supplemental Figure 10 for shear-thickening and shear-thinning liquids presents the shift in temperature profile towards space-dependent or temperature-dependent heat generation/absorption factors. As expected, increasing heat source values ($B_1, B_2 > 0$) raise the liquid temperature over the pane, but during declining, heat source values ($B_1, B_2 < 0$), the absorption of energy lessens the temperature. Supplemental Figure 11 depicts how the thermophoresis factor Nt behaves in relation to the concentration profile of nanoparticles for dilatant ($n = 1.5$) and pseudo-plastic ($n = 0.5$). Thermophoresis increases nanoparticle passage from hot surfaces to cold liquids. These increase the absorption of nanoparticles on the surface, which improves level depth.

Supplemental Figure 12 demonstrates how the Brownian motion factor Nb influences nanoparticle concentration in shear-thickening and shear-thinning liquids. The system's nanoparticles' erratic movements change the concentration field. So, the significant energy shifts and consequent

Table 3. Tabular results for skin-friction coefficient.

Λ_1	Nr	Rb	A	Nt	Nb	Rd	$NuRe^{-1/2}(2 - \beta)^{0.5}$	
							$n = 0.5$	$n = 1.5$
0.0	0.2	0.1	0.1	0.1	0.1	0.2	0.911884	0.906563
0.3							0.955586	0.947632
0.6							0.993082	0.982300
0.9							1.026088	1.012342
0.2	0.0						0.943029	0.935878
	0.4						0.940609	0.933656
	0.8						0.938168	0.931409
	1.2						0.935703	0.929137
	0.2	0.0					0.944352	0.937141
		0.2					0.939270	0.932377
		0.4					0.934100	0.927522
		0.6					0.928839	0.922572
		0.1	0.0				1.004650	0.998898
			0.2				0.876485	0.868049
			0.4				0.738135	0.726712
			0.6				0.589435	0.574848
			0.1	0.1			0.941822	0.934770
				0.3			0.875115	0.868507
				0.5			0.814169	0.807963
				0.7			0.758455	0.752614
				0.1	0.1		0.941822	0.934770
					0.3		0.823658	0.817383
					0.5		0.718860	0.713297
					0.7		0.626253	0.621333
					0.1	0.0	0.785286	0.779291
						0.4	1.086451	1.078451
						0.8	1.350012	1.340347
						1.2	1.588838	1.577734

reduction in layer thickness improve thermal performance. In contrast to shear-thinning liquid, the shear-thickening liquid gets more impacted. For shear-thickening and shear-thinning liquids, Supplemental Figure 13 demonstrates that the concentration of nanoparticles falls when the chemical reaction factor Kr is increased. Hence, the concentration of nanoparticles in this instance decreases in the permeable case. These have an impact on the humidity and temperature of agricultural fields, destroying harvests due to freezing, transferring energy primarily to a rainy cooling tower, dissipating against a water body surface, etc. We designed Supplemental Figure 14 to examine the Peclet number Pe effect on the density of motile microbes in liquids that are both shear thinning and shear thickening. This graph demonstrates how the profile of microbe density decreases with Peclet number. This occurred as a result of Peclet number Pe 's reduction of the density of microbes and the profile of their density over the whole boundary layer area.

The variations in the microorganism density profile are shown in Supplemental Figure 15 by changing the bioconvection Lewis number Lb for pseudo-plastic ($n = 0.5$) and dilatant ($n = 1.5$) materials. This graph demonstrated the relationship between the bioconvection Lewis number Lb and the diffusivity motile microbes' thickness, an inverse relationship. In contrast to

shear-thinning liquid, the shear-thickening liquid gets impacted more.

Using Table 2, we study fluctuations in skin friction coefficient versus thermo-physical factors (We , kp , λ , Nr , Rb , β , A , Λ_1) for $n = 1.5$ (shear-thickening case) and $n = 0.5$ (shear-thinning case). Table 2 shows that the skin friction coefficient has larger values in shear-thickening case. Also Wessenberg number We , porous impact kp , wedge moving factor λ , buoyancy ratio factor Nr , Rayleigh number Rb decrease the wall shear stress while wedge angle factor β , unsteady factor A and mixed convection factor Λ_1 have opposite impacts on it. Table 2 expresses that the increment rate is 67.86% for shear-thinning case, whereas shear-thickening case is 71.68% with increase of wedge angle. With the increment in porous medium, shear-thinning liquid exhibits 50.5% reduction in skin friction, whereas shear-thickening liquid confirms 51.25%.

Variations in local Nusselt number versus controlling factors (Λ_1 , Nr , Rb , A , Nt , Nb , Rd) are discussed via Table 3 for $n = 0.5$ (shear thinning) and $n = 1.5$ (shear thickening). Table 3 shows that heat transfer rate in shear-thickening case is less than the shear-thinning case. Table 3 presents that the buoyancy ratio factor Nr , Rayleigh number Rb , unsteady factor A , thermophoresis factor Nt and Brownian movement Nb reduce the Nusselt number while mixed convection Λ_1 and radiation factor

Rd enhance it. Table 3 ensures that 12.52% increment in heat transfer for pseudo-plastic liquid in mixed convection, whereas it is 11.66% for dilatant liquids. Similarly, for unsteady case the heat transfer decline is 41.32% and 42.45% for the shear-thinning and shear-thickening liquids.

Conclusions

In a porous media with heat radiation and bioconvection present, the solutions for the vacillating Falkner-Skan stream of Carreau nanoliquid across a stationary or poignant wedge have been explored. It was also considered how much heat is generated or absorbed depending on the temperature and space. Also used was a binary chemical reaction in the species concentration. The governing issue was resolved effectively using the finite element approach. The effects of significant strictures that affect the rapidity, heat, nanoparticles and motile absorption distributions are explored with regard to pseudo-plastic and dilatant liquids. The current investigation concludes:

- For pseudo-plastic and dilatant liquids, the radiation factor, Brownian motion factor, thermophoresis factor, and temperature amplify in the opposite direction for the heat absorption factor.
- The gain in the Brownian factor and the chemical reaction factor lessens the concentration and its boundary sheet, but it leads to an increase in the thermophoresis factor for shear-thickening and shear-thinning liquids, respectively.
- For both shear-thickening and shear-thinning liquids, raising the bioconvection Lewis and Peclet number reduces the thickness of movable microbes.
- Local Nusselt number exhibits stimulating behaviour against thermal radiation and mixed convection, however, Brownian motion and thermophoresis factors degrade it in magnitude sense. Shear-thickening liquids transmit heat at a slower pace than shear-thinning liquids.

Acknowledgements

The authors are very grateful to the editor and reviewers for their constructive suggestions.

Declaration of conflicting interests

The authors declared no potential conflicts of interest with respect to the research, authorship, and/or publication of this article.

Funding

The authors received no financial support for the research, authorship, and/or publication of this article.

ORCID iD

Kotha Gangadhar  <https://orcid.org/0000-0002-0264-2512>

Supplemental material

Supplemental material for this article is available online.

References

1. Kuznetsov AV. The onset of nanoliquid bioconvection in a suspension containing both nanoparticles and gyrotactic microbes. *Int Commun Heat Mass Transfer* 2010; 37: 1421–1425.
2. Hussain S, Raizah Z and Aly AM. Thermal radiation impact on bioconvection stream of nano-enhanced phase change materials and oxytactic microbes inside a vertical wavy porous cavity. *Int Commun Heat Mass Transf* 2022; 139: 106454.
3. Waqas M, Adil Sadiq M and Bahaidarah HMS. Gyrotactic bioconvection stratified stream of magnetized micropolar nanoliquid configured by stretchable radiating surface with Joule heating and viscous dissipation. *Int Commun Heat Mass Transf* 2022; 138: 106229.
4. Rana S, Mehmood R and Bhatti MM. Bioconvection oblique motion of magnetized Oldroyd-B liquid through an elastic surface with suction/injection. *Chin J Phys* 2021; 73: 314–330.
5. Ali B, Ali M, Iqrasaman, et al. Tangent hyperbolic nanoliquid: significance of Lorentz and buoyancy forces on dynamics of bioconvection stream of rotating sphere via finite element simulation. *Chin J Phys* 2022; 77: 658–671.
6. Shafiq A, Colak AB and Sindhu TN. Significance of bioconvective stream of MHD thixotropic nanoliquid passing through a vertical surface by machine learning algorithm. *Chin J Phys* 2022; 80: 427–444.
7. Gangadhar K, Lakshmi KB, Kannan T, et al. Stefan blowing on chemically reactive nano-liquid stream containing gyrotactic microbes with leading edge accretion (or) ablation and thermal radiation. *Indian J Phys* 2022; 96: 2827–2840.
8. Kushwaha AK and Sharma YD. Significance of vertical vibration on the stability of thermo-bioconvection in a suspension of oxytactic microbes. *Int Commun Heat Mass Transf* 2022; 133: 105943.
9. Rashad AM and Nabwey HA. Gyrotactic mixed bioconvection stream of a nanoliquid past a circular cylinder with convective boundary condition. *J Taiwan Inst Chem Eng* 2019; 99: 9–17.
10. Ramesh GK, Madhukesh JK, Aly EH, et al. Modified Buongiorno's model for biomagnetic hybrid nanoliquid past a permeable moving thin needle. *Int J Numer Method H* 2022; 32: 3551–3578.
11. Biswas N, Manna NK, Mandal DK, et al. Magnetohydrodynamic bioconvection of oxytactic microbes in porous media saturated with Cu-water nanoliquid. *Int J Numer Method H* 2021; 31: 3461–3489.
12. Waqas H, Imran M, Muhammad T, et al. On bio-convection thermal radiation in Darcy-Forchheimer stream of nanoliquid with gyrotactic motile microorganism under Wu's slip over stretching cylinder/plate. *Int J Numer Method H* 2021; 31: 1520–1546.
13. Nabwey HA, EL-Kabeir SMM, Rashad AM, et al. Gyrotactic microbes mixed convection stream of nanoliquid over a vertically surfaced saturated porous media. *Alex Eng J* 2022; 61: 1804–1822.
14. Elbashesy EMA, Asker HG and Nagy B. The effects of heat generation absorption on boundary layer stream of a

- nanoliquid containing gyrotactic microbes over an inclined stretching cylinder. *Ain Shams Eng J* 2022; 13: 101690.
15. Ahmad S, Akhter S, Shahid MI, et al. Novel thermal aspects of hybrid nanoliquid stream comprising of manganese zinc ferrite $MnZnFe_2O_4$, nickel zinc ferrite $NiZnFe_2O_4$ and motile microbes. *Ain Shams Eng J* 2022; 13: 101668.
 16. Hussain M, Ranjha QA, Anwar MS, et al. Eyring-Powell model stream near a convectively heated porous wedge with chemical reaction effects. *J Taiwan Inst Chem Eng* 2022; 139: 104510.
 17. Berrehal H, Dinarvand S and Khan I. Mass-based hybrid nanoliquid model for entropy generation analysis of stream upon a convectively-warmed moving wedge. *Chin J Phys* 2022; 77: 2603–2616.
 18. Ramesh GK, Shehzad SA and Izadi M. Falkner-Skan stream of aqueous magnetite-graphene oxide nanoliquid driven by a wedge. *Chin J Phys* 2022; 77: 733–746.
 19. Izady M, Dinarvand S, Pop I, et al. Stream of aqueous Fe_2O_3 -CuO hybrid nanoliquid over a permeable stretching/shrinking wedge: a development on Falkner-Skan problem. *Chin J Phys* 2021; 74: 406–420.
 20. Khan M, Sardar H and Hashim . Heat generation/absorption and thermal radiation impacts on three-dimensional stream of Carreau liquid with convective heat transfer. *J Mol Liq* 2018; 272: 474–480.
 21. Maqbool K, Manzoor N, Ellahi R, et al. Influence of heat transfer on MHD Carreau liquid stream due to motile cilia in a channel. *J Therm Anal Calorim* 2021; 144: 2317–2326.
 22. Riaz A, Abbas T and Ain AQU. Nanoparticles phenomenon for the thermal management of wavy stream of a Carreau liquid through a three-dimensional channel. *J Therm Anal Calorim* 2021; 143: 2395–2410.
 23. Afzal Q and Akram S. Impact of double-diffusivity convection in nanliquids and induced magnetic field on peristaltic pumping of a Carreau liquid in a tapered channel with different wavedorms. *J Therm Anal Calorim* 2021; 143: 2291–2312.
 24. Azam M. Bioconvection and nonlinear thermal extrusion in development of chemically reactive Sutterby nano-material due to gyrotactic microbes. *Int Commun Heat Mass Transf* 2022; 130: 105820.
 25. Sithole H, Mondal H, Goqo S, et al. Numerical simulation of couple stress nanoliquid stream in magneto-porous medium with thermal radiation and a chemical reaction. *Appl Math Comput* 2018; 339: 820–836.
 26. Madhukesh JK, Ramesh GK, Prasannakumara BC, et al. Bio-Marangoni convection stream of Casson nanoliquid through a porous medium in the presence of chemically reactive activation energy. *Appl Math Mech-Engl Ed* 2021; 42: 1191–1204.
 27. Sivasankaran S, Chandrapushpam T, Bhuvanewari M, et al. Effect of chemical reaction on double diffusive MHD squeezing copper water nanoliquid stream between parallel plates. *J Mol Liq* 2022; 368: 120768.
 28. Carreau PJ. Rheological equations from molecular network theories. *Trans Soc Rheol* 1972; 116: 99–91.
 29. Khan M, Azam M and Alshomrani AS. Unsteady slip stream of Carreau nanoliquid over a wedge with nonlinear radiation and new mass flux condition. *Results Phys* 2017; 7: 2261–2270.
 30. Mumraiz S, Ali A, Awais M, et al. Entropy generation in electrical magnetohydrodynamic stream of Al_2O_3 -Cu/ H_2O hybrid nanoliquid with non-uniform heat flux. *J Therm Anal Calorim* 2021; 143: 2135–2148.
 31. Qayyum S, Asad S and Alhussain ZA. Numerical aspects for chemical reaction on MHD stagnation point stream of Williamson nanoliquid under the effect of buoyancy force. *Arab J Sci Eng* 2022; 47: 9215–9223.
 32. Das S, Banu AS and Jana RN. Delineating impacts of non-uniform wall temperature and concentration on time-dependent radiation-convection of Casson liquid under magnetic field and chemical reaction. *World J Eng* 2021; 18: 780–795.
 33. Ray AK and Vasu B. Influence of chemically radiative nanoparticles on stream of Maxwell electrically conducting liquid over a convectively heated exponential stretching sheet. *World J Eng* 2019; 16: 791–805.
 34. Acharya N, Das K and Kundu PK. Influence of multiple slips and chemical reaction on radiative MHD Williamson nanoliquid stream in porous medium: a computational framework. *Multidisp Model Mater Struct* 2019; 15: 630–658.
 35. Yousef NS, Megahed AM, Ghoneim NI, et al. Chemical reaction impact on MHD dissipative Casson-Williamson nanoliquid stream over a slippery stretching sheet through porous medium. *Alex Eng J* 2022; 61: 10161–10170.
 36. Abbas Z, Imran M and Naveed M. Impact of equally diffusive chemical reaction on time-dependent stream of Casson nanoliquid due to oscillatory curved stretching surface with thermal radiation. *Arab J Sci Eng* 2022; 47: 16059–16078.
 37. White FM. *Viscous fluid flow*. New York: McGraw-Hill, 1991.